Propagation and rupture of elastoviscoplastic liquid plugs in airway reopening model

S. Amir Bahrani [a,*], Souria Hamidouche [a], Masoud Moazzen [a], Khady Seck [a], Caroline Duc [a], Metin Muradoglu [b], James B. Grotberg [c], Francesco Romanò [d,*]

[a] IMT Nord Europe, Institut Mines Télécom, Univ. Lille, Center for Energy and Environment, F-59000 Lille, France
[b] Department of Mechanical Engineering, Koç University, Rumelifeneri Yolu, Sariyer, 34450, Istanbul, Turkey
[c] Department of Biomedical Engineering, University of Michigan, 2123 Carl A. Gerstacker Building, 2200 Bonisteel Boulevard, Ann Arbor, MI 48109-2099, USA
[d] Univ. Lille, CNRS, ONERA, Arts et Métiers Institute of Technology, Centrale Lille, FRE 2017-LMFL-Laboratoire de Mécanique des Fluides de Lille - Kampé de Fériet, F-59000, Lille, France

ABSTRACT

The propagation and rupture of mucus plugs in human lungs is investigated experimentally by injecting synthetic mucus in a pre-wetted capillary tube. The rheology of our test liquid is thoroughly characterized, and four samples of synthetic mucus are considered in order to reproduce elastoviscoplastic regimes of physiological interest for airway reopening. Our experiments demonstrate the significant impact of the viscoplasticity and viscoelasticity of mucus. In support to our experiments, we propose a one-dimensional reduced-order model that takes into account capillarity, and elastoviscoplasticity. Our model manages to capture the cross-section averaged dynamics of the liquid plug and is used to elucidate and interpret the experimental evidence. Relying on it, we show that the liquid film thickening due to non-Newtonian effects favors plug rupture, whereas the increase of the effective viscosity due to higher yield stresses hinders plug rupture. As a result of such two effects, increasing the polymeric concentration in the mucus phase leads to a net increase of the rupture time and traveling length. Hence, non-Newtonian effects hinder airway reopening.

1. Introduction

Liquid plugs in conduits and pipes are typical flow regimes encountered in two-phase microfluidics [1]. At small scales inertial and gravitational effects play a minor role in the dynamics of the flow, while surface tension and Marangoni stresses gain an increasing importance from millimetric down to nanometric characteristic lengths. Understanding, predicting and controlling liquid plugs in confined flows is of crucial importance for designing micron-size and labs-on-a-chip devices. Moreover, the presence of liquid plugs is commonly reported in pulmonary flow due to disease or closure of distal airways and the propagation of liquid plugs plays a major role in medical treatments based on direct instillation of liquid solutions [2]. The fundamental understanding of liquid plug dynamics in pulmonary flows represents the main motivation of our study, with a special focus on the effect of non-Newtonian rheological properties of the liquid phase.

The thin liquid film lining the inner airway walls is formed by the mucus layer and the serous layer, with the latter in contact with the airway walls [3]. The dynamics of such a thin film is of major importance for the formation of liquid plugs in lungs. When the airway radius is of the order of a millimeter or smaller, the inertial and gravitational forces on the thin film represent higher-order effects and the dynamics of the film is governed, in fact, by viscous forces (in the lubrication approximation) and, in particular, by capillary forces due to surface tension. It results that, when the liquid film thickness exceeds a critical value, the liquid film may undergo a Plateau–Rayleigh instability [4,5] leading to the formation of liquid plugs across the airway lumen and preventing gas exchange for distal airways [6]. This phenomenon is termed airway closure, and it occurs in healthy subjects at the end of the expiration cycle [6,7] or in pathological conditions induced by pneumonia [8], asthma [9], bronchiolitis [10], chronic obstructive pulmonary disease (COPD [11]), cystic fibrosis [12], and acute respiratory distress syndrome (ARDS [13]).

The experimental and numerical investigations by Bian et al. [14], Tai et al. [15], and Romanò et al. [16] focused on the potential damage of airway closure on the epithelial cells. As pointed out by Grotberg [17], the mechanical stresses and strains induced on the epithelium by repetitive airway closure and reopening events can cause,

* Corresponding authors.
E-mail addresses: amir.bahrani@imt-nord-europe.fr (S.A. Bahrani), francesco.romano@ensam.eu (F. Romanò).

themselves, lung injury and disease. The protective impact of surfactant, which reduces the mean surface tension, has been experimentally and numerically demonstrated by Cassidy [18] and Halpern et al. [19], respectively. All these investigations focused on the capillary instability of the liquid film coating the airways. However, simultaneously to the Plateau–Rayleigh instability, also the elastic instability of the deformable airway wall plays an important role in the airway closure (see e.g. Halpern and Grotberg [20]). A detailed study of the interplay between interfacial and elastic instabilities is reported by Heil et al. [21], who showed that both such instabilities play in favor of the occlusion of the respiratory airways. Another element of complexity of the liquid plug formation in human lungs is due to the non-Newtonian behavior of mucus, which includes viscoelasticity [22,23], yield stress and shear-dependent viscosity (shear-thinning [24]). The non-Newtonian effects have a significant impact on airway closure as shown by Halpern et al. [25] and their characterization represents an active field of research in pulmonary fluid mechanics.

Once a liquid plug occludes the airway, the air-blown plug propagates inside the lungs, either rupturing or persisting and splitting when it encounters an airway bifurcation. The former scenario occurs when the precursor liquid film is thinner than the trailing film [26–28] . This phenomenon is called airway reopening, and it causes a pressure wave detectable by a stethoscope [29]. The reopening of respiratory airways has been extensively investigated because of its damaging effects due to very high stress levels at the airway walls. The capillary wave characteristic of the retracting air finger (see Bretherton [30], Taylor [31]) and the dynamics immediately after rupture [32] are responsible of such a high level of wall stresses and of the consequent lethal or sub-lethal response of epithelial cells [32–34]. The strong correlation between plug rupture and high wall stress levels has been confirmed by the simulations of Fujioka and Grotberg [27,35], Fujioka et al. [36], Hassan et al. [37], and Muradoglu et al. [38], who considered an airway modeled either as a rigid pipe or a rigid channel. Further confirmations are reported by the in-vivo experiments by Muscedere et al. [39] and Taskar et al. [40]. Other investigations focused on the effect of surfactant that plays a crucial role in reducing the surface tension at the liquid–air interface [41]. Fujioka and Grotberg [35] numerically investigated the effect of surfactant on the steady propagation of a liquid plug within a two-dimensional channel. The results showed that the mechanical stresses induced by the plug propagation is reduced even if the preexisting surfactant concentration is small. The same observation has been also made by Tavana et al. [42], who performed an experimental study on the effects of surfactant on cell injury. Adding a physiologic amount of Survanta, they showed that plug propagation significantly reduces the lethal response of epithelial cells. This has been confirmed by the extensive simulations of Muradoglu et al. [38], capable to reproduce the whole rupture process, including the post-rupture phase. The effect of compliance of airway walls was considered by Zheng et al. [43], who showed an enhancement of the stress level on the airway walls due to wall deformability. The effect of yield stress on plug rupture has been experimentally and numerically investigated by Hu et al. [44,45], Low et al. [46] and Zamankhan et al. [47]. They either dealt with liquid plugs on a dry or a pre-wetted channel, focusing on the dynamics of the non-Newtonian liquid plug up to the rupture event. Other numerical and experimental studies focused on a train of plugs and discussed catastrophic events in the airway network [48] or surfactant-replacement therapies where the liquid plugs are formed due to the liquid instilled into airways for medical treatment [2,49]. For literature reviews of respiratory airway closure, liquid plug propagation, and rupture, we refer to Grotberg [28,50,51].

In this paper we focus on the impact of the non-Newtonian properties of mucus on the liquid plug rupture. We perform a detailed rheological analysis of various samples of synthetic mucus and employ such samples to study airway reopening. Finally, we derive a reduced-order model to shed some light on the standalone effect of viscoplasticity and viscoelasticity. The paper is structured as follows: In Section 2 the experimental set-up and the corresponding results are described; In Section 3 we define the framework of our reduced-order model, derive such a model based on up-to-date correlations reported in literature, and presents the corresponding results; finally, the conclusions of our study are drawn in Section 4.

2. Experiments

2.1. Synthetic mucus samples

The synthetic mucus used in this study is a compound of water and two polymers. The Scleroglucan Polysaccharide (Actigum®) is employed as a chemical agent to increase the liquid viscosity and Locust Bean Gum (Vidogum® L-175) is used as a thickening agent. We dissolve 0.25 g of Vidogum in 50 ml of distilled water for 2 h and then different Actigum concentrations ($\tilde{c}_{\mathrm{act}}$ = 0.25, 0.5, 1 and 1.5 g/ml.) are added to such aqueous solutions. Copper sulfate $CuSO_4$ (0.05 g) is also added as a stabilizer before keeping the mixtures under agitation conditions for 24 h at room temperature (around 21 °C). After that, the aqueous solutions are left at rest for 24 h in order to recover the gel structure before performing any other manipulation. The solutions are stocked in close containers that prevent significant evaporation as they are stored at 4 °C. In the followings, we name them after their characteristic Actigum concentrations, i.e., MUC-0.25%, MUC-0.5%, MUC-1% and MUC-1.5% correspond to $\tilde{c}_{\mathrm{act}}$ = 0.25, 0.5, 1 and 1.5 g/ml, respectively.

As aforementioned, we use vidogum and $CuSO_4$ for preparing our synthetic mucus. This is different from the experimental protocol proposed by Lafforgue et al. [52], who rather employ viscogum and NaCl. We stress that our choice of $CuSO_4$ instead of NaCl is intended to avoid the spontaneous development of microbiological culture through the synthetic mucus. As a result, the lifetime of the final aqueous solutions is increased.

2.2. Rheological measurements

The rheological behavior of the synthetic mucus is characterized using a cone/plate geometry (50 mm/1°) with truncation gap of θ = 0.104 mm. All measurements are carried out in an Anton-Paar MCR 302 rheometer at a constant temperature of 21 °C. Two flow sweep protocols are applied to measure the rheological characteristics of the synthetic mucus and the relaxation time. At first, in order to find viscosity and fitting Herschel–Bulkley model the flow curve measurement was done. This was happened by following a standard protocol of flow sweep [53,54] within the shear-rate interval of $0.01/\mathrm{s} < \dot{\gamma} < 1000/\mathrm{s}$. Then to get the dynamic, shear rate dependent, relaxation time λ, we followed step by step the protocol detailed by Casanellas et al. [55]. This experimental protocol is consisted of several incremental steps. In each step a constant shear rate is imposed with multiple measuring points. Right-after a flow sweep test is conducted where the solution was sheared at a small shear rate of reference ($\dot{\gamma} = 1s^{-1}$). On each step, subtracting the means of two values of the first normal stress difference N_1 gives a way to resolve the instrumental drift of the normal force and find real value of $N_1(\dot{\gamma})$. This latter will be completed by removing the contribution of fluid inertia to the normal force. Moreover, it can clarify the non-linear rheological behavior of the different samples in which the real rheological response of the samples is shear-rate dependent.

A shear-thinning behavior is observed for all the aqueous solutions. The resulting rheological curves are characterized by fitting the Herschel–Bulkley model, $\tau = \tau_0 + K\dot{\gamma}^n$, where τ, τ_0, K, and n are the shear stress, yield stress, consistency index, and power-law index, respectively (see Fig. 1). The rheological parameters of the synthetic mucus solutions are summarized in Table 1. The results show that the yield stress for MUC-0.25% is 0.59 Pa and it increases upon an increase of the Actigum concentration ($\tilde{c}_{act}$). A similar trend is also observed for the consistency index, the power-law index, n, slightly decreases as $\tilde{c}_{\mathrm{act}}$

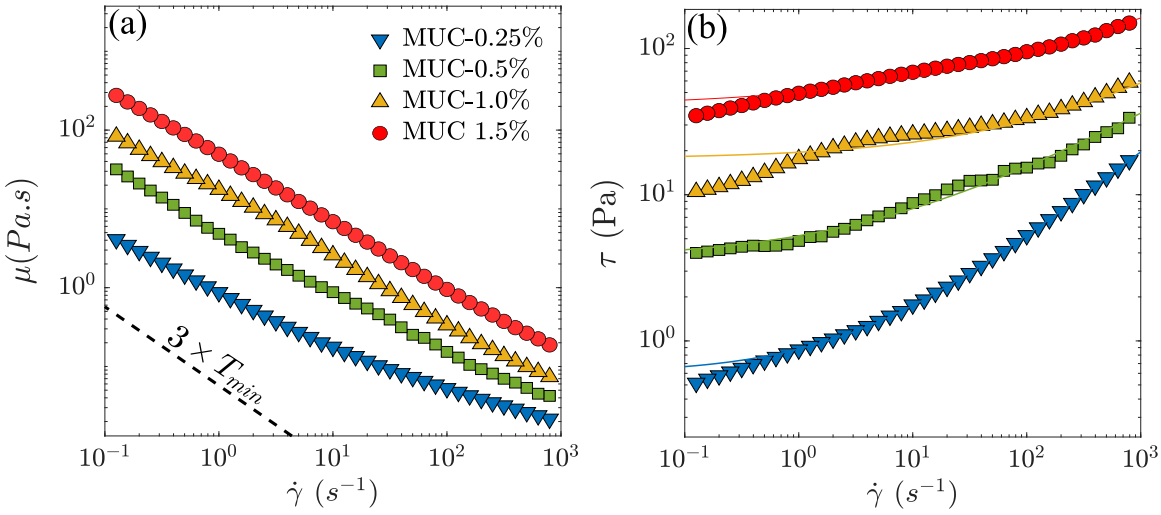

Fig. 1. Flow curves of the synthetic mucus solutions obtained from rheological measurement at 21 °C. (a) Viscosity *vs* shear rate. The dashed line represents the rheometer low-torque limit which is multiplied by 3 ($\mu < 3T_{min}/(2\pi R_1^3\dot{\gamma})$, with R_1 = 50 mm and T_{min} = 0.5 μN m [57]). (b) Shear stress *vs* shear rate. The colored continuous lines represents fits based on the Herschel–Bulkley model applied to flow curves. The discrepancy between fits and the experimental results is attributed to slip of solution in low torques.

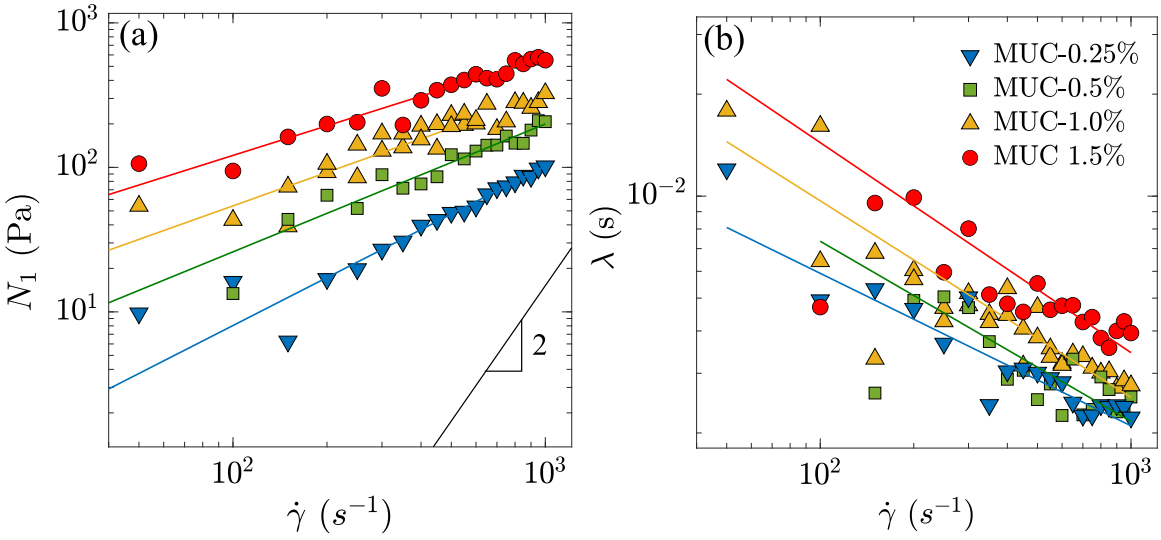

Fig. 2. (a) First normal-stress difference as a function of shear rate. Data are fitted with a power law model. Black solid line of slope $\alpha = 2$ represents the Oldroyd-B model ($N_1 = 2\eta_p\lambda\dot{\gamma}^2$), considering an identical relaxation time at polymer contribution to the zero shear viscosity η_p. (b) Relaxation time as a function of shear rate for different concentration of synthetic mucus using the White–Metzner model. Colored continuous lines are fitted to the experimental data by a power law model. The corresponding model constants can be found in Table 1.

Table 1
Rheological parameters of the synthetic mucus suspensions derived by fitting the Herschel–Bulkley model $\tau = \tau_0 + K\dot{\gamma}^n$ as well as the White–Metzner model [56] in order to find the relaxation time, λ. All solutions follow the relations of $N_1 \propto \dot{\gamma}^\alpha$ and $\lambda \propto \dot{\gamma}^\beta$, where the exponents α and β govern the viscoelastic behavior of the solutions.

Sample	Herschel–Bulkley model			viscoelastic behavior	
	τ_0 (Pa)	K	n	α	β
MUC - 0.25%	0.59	0.28	0.61	1.10	−0.45
MUC - 0.5%	3.60	1.64	0.43	0.88	−0.53
MUC - 1%	17.63	1.88	0.44	0.77	−0.59
MUC - 1.5%	40.08	10	0.36	0.68	−0.62

increases. This shows that the solutions become more shear-thinning as $\tilde{c}_{act}$ increases.

The viscoelastic behavior of the synthetic mucus can be described by employing various rheological models. One way is to assume that the relaxation time is independent of the shear rate. This approach is typically employed in the Oldroyd-B, the FENE-P and FENE-CR models, applied generally to solutions with low concentration of polymers. However, in the case of non-linear rheological behavior, likely for higher polymer concentrations, we can use the White–Metzner constitutive equation [56]. This model (see Eq. (1)) assumes that the relaxation time, shear viscosity and first normal-stress difference N_1 are shear-dependent

$$N_1 = 2\left[\eta(\dot{\gamma}) - \eta_s\right]\lambda(\dot{\gamma})\dot{\gamma}^2 \tag{1}$$

where $\eta(\dot{\gamma})$ and $\lambda(\dot{\gamma})$ are the shear rate dependent total viscosity and relaxation time, respectively, and η_s is the solvent viscosity. The difference, $\eta(\dot{\gamma}) - \eta_s$, gives the polymer viscosity contribution η_p. Finally, we can calculate the relaxation time by rewriting (1) to isolate $\lambda(\dot{\gamma})$ by introducing the ratio of the first normal-stress difference N_1 to shear stress $\sigma = \eta(\dot{\gamma})\dot{\gamma}$

$$\lambda(\dot{\gamma}) = \frac{1}{2\dot{\gamma}}\frac{\eta(\dot{\gamma})}{\left(\eta(\dot{\gamma}) - \eta_s\right)}\frac{N_1}{\sigma} \tag{2}$$

Fig. 2 shows the results of the normal stress difference and relaxation time as a function of shear rate. Note that N_1, σ and $\eta(\dot{\gamma})$

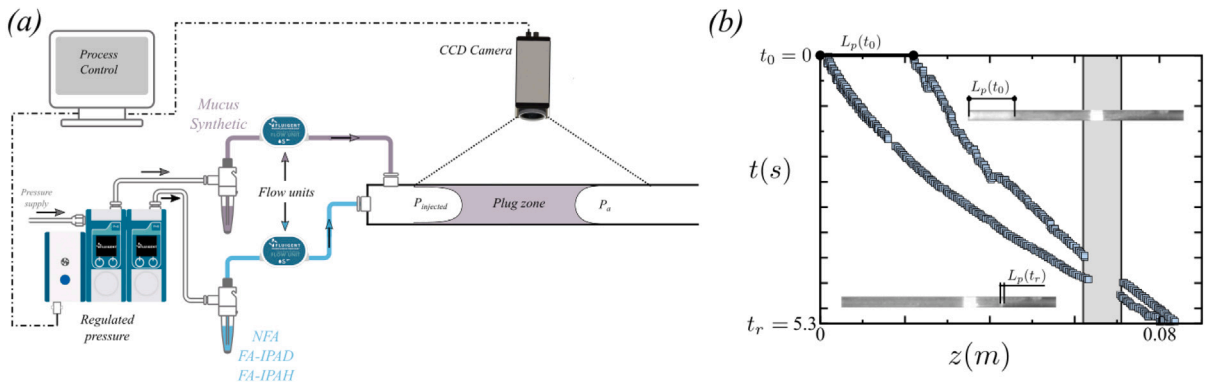

Fig. 3. Sketch of the experimental apparatus. (a) Experimental set-up. (b) Tracking of the rear and the front menisci, and space–time diagram.

are obtained experimentally using the rheometer. However, as already mentioned, the raw data of N_1 was corrected by subtracting the inertial contribution. This was done by subtracting the negative inertial effect which tends to pull down the cone due to the presence of liquid between the cone-plate rheometer instrument [58]. The corresponding correction is given by: $N_1 = N_{1,tot} + 0.15\rho\Omega^2R^2$, where $N_{1,tot}$ is the total/row normal-stress difference directly given by the rheometer and $\Omega = \tan(\theta)\dot{\gamma}$ is the angular velocity. It is worth to mention that these corrections rely on the accurate measurements of N_1. This latter depends on resolution of the normal force sensor of the rheometer, especially at the low polymer concentrations and shear rates. As can be seen in Fig. 2(a) the evolution of N_1 as a function of shear rate shows a power law like $N_1 \propto \dot{\gamma}^{\alpha}$. The results show that the slope of α decrease by increasing of shear-thinning degree depending on the concentration of Actigum $\tilde{c}_{\text{act}}$ (see Table 1). Indeed the value of α determines the complexity of non-linear rheological response of the fluids, for $\alpha = 2$, the behavior follows the Oldroyd-B model. The relaxation time as a function of shear rate (1)b is also represented by a power law function as $\lambda \propto \dot{\gamma}^{\beta}$. The values of β, summarized in Table 1, indicate larger relaxation times as the concentration of Actigum increases. Fig. 2 also demonstrates that as the shear-thinning degree increases the relaxation time becomes more sensible to shear rate.

2.3. Experimental apparatus

The experiments of a liquid plug propagation in a pipe flow were conducted using a cylindrical glass tube with inner diameter of $d_i = 2a = 4$ mm corresponding to the diameter of bronchioles at 6th-to −7th generation of an adult human lung. In order to reproduce the dynamics of a liquid plug, a controlled volume of the synthetic mucus is injected, at first, through the glass tube, and then pushed along using two different gases as described in detail below.

The mucus and gas injections are performed at a constant flow rate by using a flowmeter (Flow Unit, Fluigent), as shown in Fig. 3(a). A systematic pre-wetting surface treatment of the glass tube is done by cleaning with acetone, isopropanol and dichloromethane before each experiment. The impact of the rheological properties of synthetic mucus is studied under atmospheric conditions, using filtered air directly coming from the room.

The dynamic rupture of liquid plugs was recorded using a CCD camera (DMK 23U618, Monochrome, up to 120 images/s, The Imaging Source, Bremen, Germany) connected to a PC. The color difference between the liquid plug (white) and the background (dark gray) is exploited in our in-house Matlab® code to post-process the dynamics of the liquid plug (see Fig. 3(b)). Each snapshot is processed by extracting a stripe of the width of one pixel along the projection of the pipe axis. The corresponding space–time diagram is thereafter obtained by gathering all the one-pixel stripes and sorting them in chronological order. As the background of the experimental setup is dark-gray and the liquid plug is white, the dynamics of the liquid plug is readily identified as illustrated in Fig. 3(b). A final image polishing is performed by using an in-house front-identification algorithm that takes advantage of the sharpness of the space–time diagram, and it characterizes the brightness contour between the white pixels of the plug and the dark-gray pixels of the background. Within this final post-processing step, we also remove the blind region of the space–time diagram (see vertical gray stripe in Fig. 3(b) due to a metallic plate employed in our experiment to hold the capillary pipe in place). The image-processing protocol readily provides the parameters of interest in our statistics, i.e. the initial plug length, $L_{\text{i}} = L_{\text{p}}(t = t_0)$, the final plug length, $L_{\text{f}} = L_{\text{p}}(t = t_{\text{r}})$, the rupture time, t_{r}, and the distance covered by the plug before the rupture event takes place (rupture length $L_{\text{r}} = z(t = t_{\text{r}})$). A schematic of such quantities is presented in Fig. 3(b). Finally, the average plug velocity is estimated by the ratio of the rupture length to the rupture time, i.e. $\overline{U}_{\text{p}} = L_{\text{r}}/t_{\text{r}}$.

2.4. Dynamics of plug ruptures

The dynamics of the liquid plug in the capillary tube is characterized for several flow conditions using the four samples of synthetic mucus and varying the initial plug length L_{i}. Fig. 4 depicts the space–time diagram of the liquid plug rupture for two different concentrations, i.e. MUC-0.5% and MUC-1.5%, and three different initial plug lengths, $L_{\text{i}} = 5$, 13 and 22 mm. The markers denote the data resulting from our image post-processing protocol, and the dashed lines are cubic polynomials obtained by least-squares fit for tracking the rear and the front menisci. Cubic polynomials are employed because they result in a smooth and seamless interpolation while avoiding oscillations known as Runge phenomena [59]. Each subfigure includes two insets representing two experimental snapshots where the plug moves from left to right. On the top-right corner we depict the liquid plug as soon as both front and rear menisci entered the observation window of our experimental setup. This condition defines $L_{\text{i}} = L_{\text{p}}(t = 0)$. On the bottom-left corner we depict the liquid plug right before rupture and we identify the final plug length $L_{\text{f}} = L_{\text{p}}(t = t_{\text{r}})$. Hence, the time taken to pass from $L_{\text{p}} = L_{\text{i}}$ to $L_{\text{p}} = L_{\text{f}}$ is the rupture time t_{r}. The white stripe at about two thirds from the pipe inlet (see Fig. 3(b)) is a fixed metal plate employed to hold the capillary tube in place. Due to it, the plug cannot be detected when passing below such a metal plate (gray stripe in Fig. 4).

The four panels of Fig. 4 report four representative experimental space–time diagrams. Fig. 4(a) shows a typical space–time diagram observed for short plugs ($L_{\text{i}} = \mathcal{O}(a)$). Regardless of the Actigum concentration, the short plugs of our experiments always rupture following an axi-symmetric dynamics. The progressive drainage of the plug up to $L_{\text{p}}(t_{\text{r}}) = L_{\text{r}} \approx 0$ is also observed for low Actigum concentrations, i.e. MUC-0.25% and MUC-0.5%, regardless of the initial plug length. This is demonstrated in Fig. 4(b). Upon an increase of the Actigum

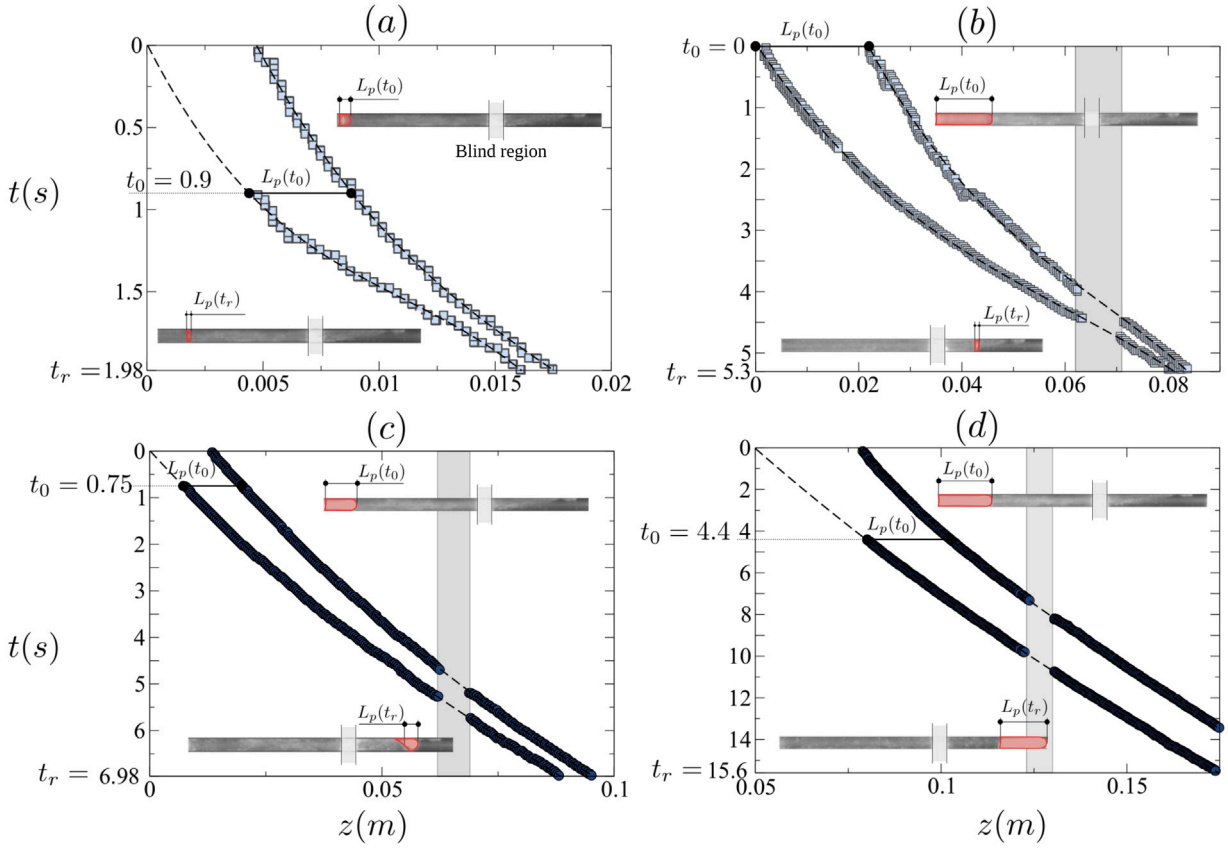

Fig. 4. Space–time diagram of the liquid plug rupture for (a, b) MUC-0.5% and (c, d) MUC-1.5%, and three initial plug lengths, i.e. (a) $L_p(t_0) = L_i = 5$, (c) 13 and (b,d) 22 mm. The markers denote the post-processed data along the pipe centerline, the dashed lines are least-squares cubic fits. Top-right inset: snapshot of the liquid plug as soon as the front and the rear menisci entered the observation window. Bottom-left inset: snapshot of the liquid plug rupture (a–c) or exit of the liquid plug from the observation window. The identified contour of the liquid plug is highlighted in red.

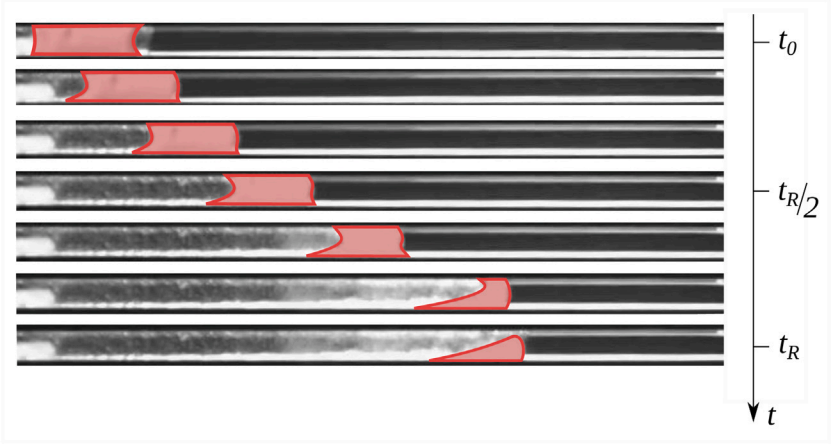

Fig. 5. Development of an asymmetric plug propagation for MUC-1.0% and $L_p(t_0) = L_i = 13$ mm.

concentration, the liquid plug becomes more prone to asymmetric ruptures (see bottom-left inset of Fig. 4(c)). A detailed dynamics of the asymmetric plug rupture for MUC-1.0% and $L_i = 13$ mm is depicted in Fig. 5. By increasing the viscoplastic character of the liquid plug, the deposition of the liquid film becomes wavy and loses the axi-symmetry observed for low Actigum concentrations. This same phenomenon has been reported in figs. 14 to 16 by Caliman et al. [60] and it results in a non-zero centerline plug length at rupture (see also space–time diagram of Fig. 4(c)). Another scenario is finally depicted in Fig. 4(d): A long liquid plug undergoes an initial drainage and then gets steadily advected in the capillary pipe without rupturing.

Fig. 6 depicts the experimental findings for our four samples of synthetic mucus upon a change of the average plug speed $\overline{U}_p$, the effective viscosity μ, the relaxation time λ, and the yield stress τ_0. Two quantities are employed for characterizing the dynamics of the liquid plug: (i) the rupture length non-dimensionalized by the difference between initial and final length $L_r/(L_i - L_f)$ and (ii) the rupture time. The first non-dimensional group is employed to compare the distance traveled by a liquid plug with the total plug-length reduction until the rupture. Fig. 6(a,b) show increasing the average plug length does not correlate with a change of non-dimensional plug length, but it rather impacts on the rupture time. This is a combined effect of (i) the faster propagating

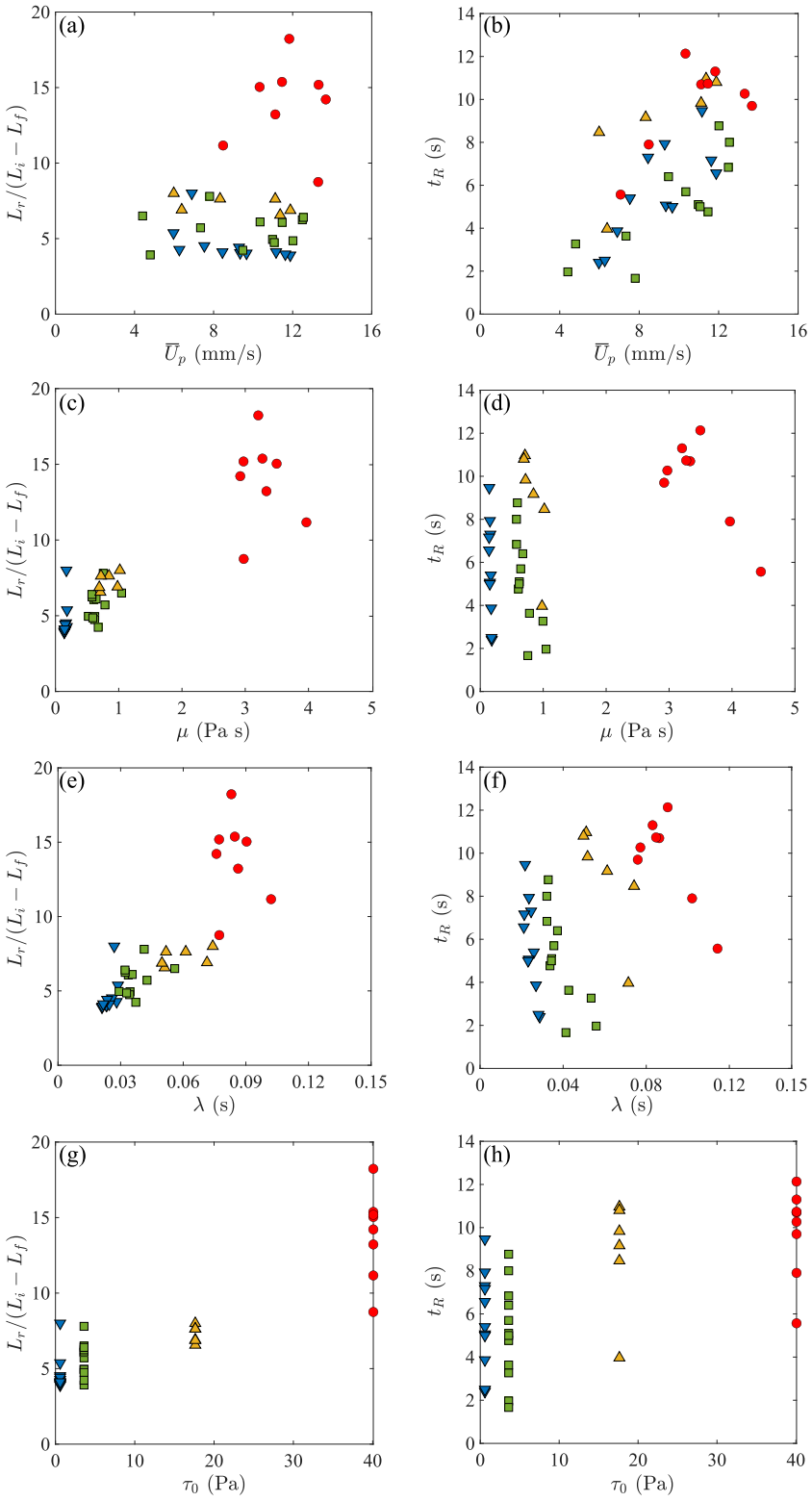

Fig. 6. Rupture time t_R (right) and non-dimensional rupture length $L_r/(L_i - L_f)$ (left) plotted against: the average plug speed $\overline{U}_p$ (a, b), the effective viscosity μ (c, d), the relaxation time λ (e, f), and the yield stress τ_0 (g, h). Same color coding of Fig. 2 is employed.

plug that experiences higher capillary numbers, hence thicker coatings, and (ii) the higher-strained plug with therefore a lower effective viscosity (shear thinning) and lower relaxation times (see Figs. 1 and 2). Also the yield stress plays a role in delaying the rupture, even if the component of the delay due to higher yield stresses seem to be a higher-order correction when compared to the capillary-number effect. The change of the plug rheology is rather more impactful on the normalized rupture length, that grows upon an increase of μ, λ and τ_0. This is consistent with the physiological observations of non-Newtonian mucus plugs that develop a higher resistance to rupture when the polymeric concentration is increased. We further stress that our trend for t_r is in agreement with the results of Hu et al. [44], who showed that the liquid

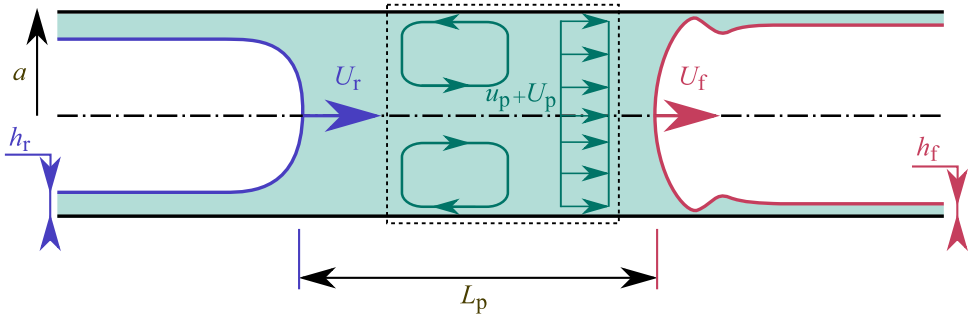

Fig. 7. Schematic of the reduced-order model for the liquid plug rupture in an airway of constant radius a. The rear air finger (dark blue) has a film thickness h_r and moves with tip velocity U_r, while the front air finger (dark red) has a film thickness h_f and recedes with tip velocity U_f. The core fluid (dotted box) is described by the recirculating flow u_p superposed to the averaged velocity $U_p = (U_r + U_f)/2$.

plug takes a longer time to deform and rupture at higher Bingham numbers. Therefore, they attributed the longer rupture time to the slowed plug deformation induced by high yield stresses. Moreover, a larger scatter of the experimental data is observed when $\tilde{c}_{act} \uparrow$, which is due to a higher probability to run into an asymmetric rupture of the liquid plug.

3. Reduced-order model of the liquid plug rupture

A reduced-order model of our experiment is formulated as a one-dimensional model based on the concept of flow resistance across a liquid plug. Referring to Fig. 7, we assume that the pressure in the advancing air finger at the trailing meniscus (rear film, subscript r) of the liquid plug, P_r, and the pressure in the receding air finger at the leading meniscus (front film, subscript f) of the liquid plug, P_f, are constant. The liquid plug moves therefore under the effect of a given pressure difference across the plug, $\Delta P = P_r - P_f$. This imposed pressure difference is opposed by the pressure drop ΔP_p due to the capillary and viscous forces. In the absence of inertia, the pressure drop is proportional to the liquid flow rate Q and can be written as $\Delta P_p = R_p Q$, where R_p is the liquid plug resistance. Assuming that the front and the rear menisci do not interact, the resistance of the plug can be expressed as a system of three resistances in series, i.e. $R_p = R_r + R_c + R_f$, where R_r and R_f are the resistances due to the interaction of surface tension with the viscous rear and front thin film, respectively, and R_c is the viscous resistance of the core. Similar modeling approaches have been proposed in literature by Howell et al. [61] and Waters and Grotberg [62], who treated the plug core inviscid, and relegated the resistance to the thin films ahead and behind the liquid plug.

Following the model of Fujioka et al. [63] for a clean Newtonian liquid plug, the following system of ODEs can be used to represent the plug propagation.

$$\frac{d}{dt}\begin{bmatrix} Z_p \\ U_p \\ L_p \end{bmatrix} = \begin{bmatrix} (U_r + U_f)/2 \\ \left(\Delta P - R_p U_p \pi a^2\right)/\rho L_p - (U_p/L_p) d_t L_p \\ \varepsilon_f (2 - \varepsilon_f) U_f - \varepsilon_r (2 - \varepsilon_r) U_r \end{bmatrix}, \tag{3}$$

where ρ is the density of the liquid, t is the time, U_p, U_r and U_f are the plug, rear-bubble and front-bubble velocities, respectively, L_p is the plug length, and $\varepsilon_r = h_r/a$ and $\varepsilon_f = h_f/a$ are the non-dimensional rear and front liquid film thicknesses, respectively (see Fig. 7). The first equation describes the location of the center of the liquid plug, Z_p, with $dZ_p/dt = U_p$, the second equation is derived from the one-dimensional Navier–Stokes equation, and the third one is the continuity equation. A detailed characterization of the Newtonian resistances is reported in the following section, partially modifying the model of Fujioka et al. [63] to take into account the recirculation resistance in the liquid plug (see u_p in Fig. 7). The derivation of the last two equations is briefly summarized in Appendix. We further generalize this model by including non-Newtonian effects. Such extension of the model of Fujioka et al. represents an original contribution of our study.

3.1. Newtonian plug resistance

A Newtonian liquid plug travels in a capillary tube of radius a and is characterized by trailing and a leading film thicknesses h_r and h_f, respectively, a length L_p and a mean traveling velocity U_p. Under the hypothesis that the rear and the front menisci do not interact, the rear meniscus can be characterized by the Bretherton lubrication model of a steady Taylor bubble advancing with velocity U_r. The pioneering work of Bretherton [30] is concerned with asymptotically small capillary numbers of the rear meniscus, i.e. $Ca_r = \mu U_r/\sigma \to 0$, where σ is the surface tension at the liquid–gas interface and μ is the dynamic viscosity of the liquid phase. The results of Bretherton [30] have successively been extended by several other authors that corrected the Bretherton's correlation for finite Ca_r. The most refined correction has recently been proposed by Fujioka et al. [63], who confirmed the formula given by Aussillous and Quéré [64] for the steady film thickness h_r and improved the result for the resistance R_r by fitting Stokesian numerical simulations of an advancing, steady, semi-infinite Bretherton bubble. The formulae by Fujioka et al. [63] read

$$\begin{aligned} \varepsilon_r &= \frac{h_r}{a} = \frac{1.34 Ca_r^{2/3}}{1 + 1.34 \times 2.5 Ca_r^{2/3}}, \\ R_r &= \frac{\mu}{\pi a^3 \left(1 - \varepsilon_r\right)^2}\left(\frac{2 \times 1.79 \times 2^{2/3} Ca_r^{-1/3}}{1 + 1.41 Ca_r^{1/3}} + 1.1\right). \end{aligned} \tag{4}$$

The film resistance of the front meniscus is considered by the correction proposed by Fujioka et al. [63] that takes into account a finite capillary number and does not require $h_f \ll a$. The formula derived by fitting the Stokes flow for a rear front of a semi-infinite Bretherton bubble is

$$\begin{aligned} R_f &= \frac{\mu}{\pi a^3 \left(1 - \varepsilon_f\right)^2}\left(-2 \times 3^{2/3} f Ca_f^{-1/3}\right), \\ f &= \sum_{k=0}^{5} C_k \left(\log_{10} \alpha\right)^k + \frac{1.02 \varepsilon_f^{0.348} \alpha^{-0.594}}{1 + 0.0778 \alpha^{-0.594}} \end{aligned} \tag{5}$$

where $Ca_f = \mu U_f/\sigma$, U_f is the velocity of the front bubble, $\varepsilon_f = h_f/a$, $\alpha = \varepsilon_f/\left(3Ca_f\right)^{2/3}$, $C_0 = -0.149$, $C_1 = 2.04$, $C_2 = 0.570$, $C_3 = 0.233$, $C_4 = 0.064$, and $C_5 = 0.00689$.

The last component of the liquid plug resistance is R_c that is obtained following the approach of Che et al. [65], who considered the recirculating axisymmetric flow $\vec{u}_p$ in the reference frame co-moving with the plug at speed U_p. Since a change of reference frame does not affect the flow resistance, we employ the formula reported in Che et al. [65]

$$R_c = -\frac{2\mu L_p}{\pi^2 a^4} \sum_{n=1}^{\infty} \frac{1 - (-1)^n}{n} \alpha_n \beta_n, \quad \alpha_n = \frac{2[(-1)^n - 1]}{n\pi\phi_n}, \quad \beta_n = -\frac{2n\pi a I_1\left(\frac{n^2\pi^2 a^2}{L_p^2}\right)}{L_p I_2\left(\frac{n^2\pi^2 a^2}{L_p^2}\right)}$$

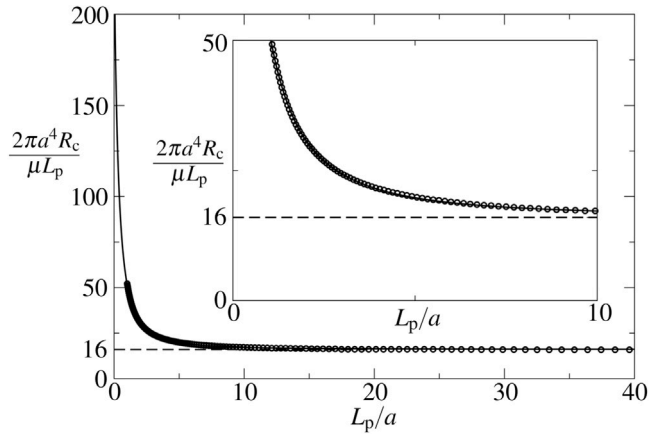

Fig. 8. The markers are derived from the resistance formula in form of infinite series (6), data extracted from fig. 8 by Che et al. [65], while the solid line is obtained from the power-law fit (7). The dashed line denotes the Hagen–Poiseuille asymptote $\lim_{L_p/a\to\infty} 2\pi a^4 R_c/\mu L_p = 16$. The inset depicts a cutout of the interval $L_p/a \in [0,\ 10]$.

$$\phi_n = \frac{n\pi a I_0\left(\frac{n\pi a}{L_p}\right) I_2\left(\frac{n\pi a}{L_p}\right) - n\pi a I_1^2\left(\frac{n\pi a}{L_p}\right)}{L_p I_1^2\left(\frac{n\pi a}{L_p}\right)} \tag{6}$$

where I_0, I_1 and I_2 are the modified Bessel function of the first kind of order 0, 1 and 2, respectively. The core resistance reported in (6) assumes straight menisci, dry plug transport and tends to the viscous resistance of a fully-developed Hagen–Poiseuille profile for long liquid plugs, i.e. $L_p \gg a$. Owing to the slow convergence of (6), it is computationally expensive to evaluate the infinite series, hence we rather prefer to employ a least-square fit built on the following power law

$$R_c = \frac{\mu L_p}{2\pi a^4}\left[16 + 77.9725\left(\frac{L_p}{a} + 0.5546\right)^{-1.7670}\right], \tag{7}$$

where the Hagen–Poiseuille asymptote enters enforcing the first coefficient of the fit, i.e. 16. A comparison between (6) and (7) is reported in Fig. 8.

3.2. Corrections for non-Newtonian effects

The effect of the non-Newtonian behavior of the liquid phase modifies all three flow resistances of our reduced-order model. To the best of the authors' knowledge, no empirical, numerical or theoretical correlations are present in the literature for taking into account the viscous, elastic and plastic behavior of the mucus simultaneously. In our model, therefore, we assume that the viscoelastic and viscoplastic corrections can be superposed.

Following Gauri and Koelling [66], the viscoelasticity of a liquid strongly affects the film thickness. Based on their experimental measurements, they propose the following correction to pass from the Newtonian to the viscoelastic (VE) case

$$\varepsilon_*^{VE}(2-\varepsilon_*^{VE}) = \varepsilon_*(2-\varepsilon_*)[0.1217\ln(De_*) + 0.8461] \tag{8}$$

where $De_* = 2U_*\lambda/a$ is the Deborah number and λ is the relaxation time of the liquid. This correlation is valid for $De_* \geq 3$, and higher-order corrections required for $De_* < 3$ are neglected in our model. No viscoelastic correction is taken into account for the core resistance. This is consistent with the limit of the Hagen–Poiseuille profile for long plugs.

Several studies have focused on the correction of the rear- and front-bubble resistances and the corresponding non-dimensional thicknesses for Herschel–Bulkley liquids (see e.g. Laborie et al. [68] and Jalaal and Balmforth [69]). However, a comprehensive explicit correlation for R_p and ε_* between Newtonian and Herschel–Bulkley liquids (hence as a function of K, τ_0, and n) is still missing. Hence, we limit the viscoplastic correction of our model to Bingham fluids ($n = 1$) and correct the film thickness and the plug resistance by fitting the results of Zamankhan et al. [47,67]. In this case Ca_* reduces to the classic definition $Ca_* = \mu U_*/\sigma$. The resulting corrections are

$$\Delta P_p^{VP} = \Delta P_p + 2.3 Bi_p \frac{\mu U_p}{a}, \tag{9a}$$

$$\frac{\varepsilon_*^{VP}(2-\varepsilon_*^{VP})}{\varepsilon_*(2-\varepsilon_*)} = 1 + \frac{Bi_*}{Ca_*}\left\{0.06\left[\tanh\left(\frac{20 - Bi_*/Ca_*}{\pi}\right) + 1\right] + 0.03\left[\tanh\left(\frac{Bi_*/Ca_* - 20}{\pi}\right) + 1\right]\right\} \tag{9b}$$

where Bi is the Bingham number $Bi_* = \tau_0 a/\mu U_*$, τ_0 is the yield stress, and the fits are reported in Fig. 9. In our fitting model, the control parameter Bi/Ca plays a relevant role in describing the viscoplastic correction of the thin film thickness. To better understand it, we consider the dynamics of a thin liquid film, i.e. $\varepsilon = h/a \ll 1$. Within the framework of the thin-film approximation, the pressure inside the liquid film is simply projected in direction normal to the wall. Hence, to leading order, the pressure inside the liquid (p relative to the air core pressure) is $p_\sigma = \sigma/(a-h) \approx \sigma/a$. For slow viscoplastic liquid plugs, and especially in the thin film coating the capillary pipe, inertial effects are negligible and the film thickness results out of the balance between viscoplasticity (hence yield stress τ_0), capillary pressure (p_σ) and viscous stresses ($\tau_v = \mu U_*/a$). Hence, the ratio between the Bingham number $Bi = \tau_0 a/\mu U_*$ and the capillary number $Ca = \mu U_*/\sigma$ represents a dimensionless group that quantifies the relative importance of yield and capillary-induced normal stresses inside the liquid film against the viscous stresses, i.e. $Bi/Ca = \tau_0 p_\sigma/\tau_v^2$. In this sense, the non-dimensional group Bi/Ca represents a parameter that involves all the stresses relevant for the dynamics of a viscoplastic thin film. The choice of Bi/Ca as a control parameter is confirmed by the data of the independent study of Zamankhan et al. where data almost collapse on the Bi/Ca–dependent fitting curve employed by our model. Considering that three very different capillary numbers have been simulated for producing the data used in Fig. 9, the remarkable data collapse is a strong indication that Bi/Ca is a significant control parameter. We stress that the ranges of capillary and Bingham numbers used in the original study of Zamankhan et al. and fitted in (8) cover the range of physiological Ca and Bi of interest for the reopening of a distal airway. In this sense, the fit is expected to be general for the purpose of its application.

Since the elastoviscoplastic corrections include a change of the non-dimensional film thicknesses, two variants M1 and M2 of the reduced-order model should be taken into account. When the thickness of the liquid films is corrected, either we consider the bubble-tip velocity constant (model M1) or we assume that the flow rate does not change (model M2). Further details are provided in the following subsection.

3.3. Algorithm of the reduced-order model

We model the liquid plug rupture of an elastoviscoplastic liquid plug assuming:

(a) A fully-developed flow profile in the liquid plug core;
(b) Superposition of viscoelastic- and viscoplastic-induced corrections for the non-dimensional film thickness of the advancing and the retracting air fingers;
(c) Correction of the capillary resistances of the liquid plug menisci determined by the viscoplastic dynamics of a Bingham fluid.

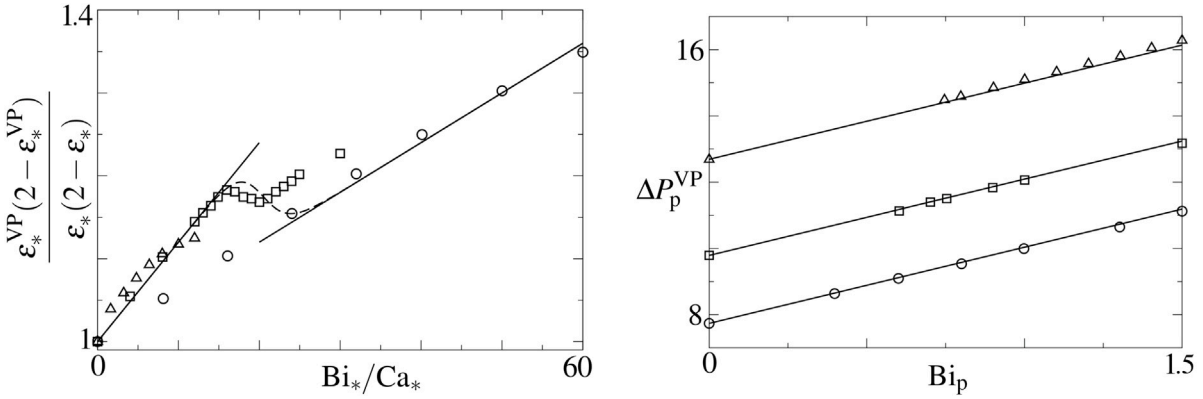

Fig. 9. Effects of viscoplasticity. The solid lines in the left panel denote the two asymptotes observed for $Bi_*/Ca_* < 20$ and $Bi_*/Ca_* > 20$, the dashed line includes the smoothed transition between them and depicts (9)(b), the solid lines in the right panel depict the fit (9)(a),while the markers are the data of Zamankhan et al. [47,67]. Left panel: Non-dimensional film thickness for $Ca = 0.25$ (triangles), $Ca = 0.1$ (squares), and $Ca = 0.05$ (circles) taken from Zamankhan et al. [67]. Right panel: Non-dimensional pressure drop for $Ca = 0.025$ (triangles), $Ca = 0.05$ (squares), and $Ca = 0.025$ (circles) taken from Zamankhan et al. [47].

The following algorithm defines our reduced-order model for an elastoviscoplastic liquid plug:

1. Enforce the front-bubble film thickness $\varepsilon_f = \varepsilon_f^{EVP}$;
2. Enforce the Bingham-to-capillary ratio and the Deborah number of the front-bubble, i.e. Bi_f/Ca_f and De_f, respectively;
3. Remove the effect of the fluid elastoviscoplasticity by inverting Eqs. (9)(right) and (8) to compute the non-dimensional film thickness of a bubble retracting in a Newtonian liquid ε_f;

Note: We test two variants for the non-Newtonian film thickness corrections (superscript corr) of the reduced-order model:

M1: velocity-matched model $U_f^{corr} = U_f$ with $\Delta P_f = -2\sigma f(3Ca_f)^{2/3}/a$;

M2: flow-rate-matched model $U_f^{corr} = U_f[(1-\varepsilon_f)/(1-\varepsilon_f^{surf})]^2$ with $\Delta P_f = -2\sigma f(3Ca_f)^{2/3}/a$;

4. Compute the capillary number and the film thickness of the front bubble by inverting (4)(left), which holds for retracting bubbles, too;
5. Compute the front-bubble velocity U_f from the capillary number of a Newtonian bubble;
6. Compute the pressure drop of a Newtonian bubble at the front-bubble tip using ΔP_f;
7. Based on the selected Bi_f/Ca_f and De_f, compute the corresponding τ_0 and λ;

Note: U_f and ΔP_f are derived by the enforced front-bubble film thickness ε_f, and by the rheological properties of mucus. Hence, none among U_f, ΔP_f and ε_f is affected by the liquid plug dynamics;

8. Compute the variation in time of the liquid plug velocity by using the following algorithm:

(viii.a) Compute the core pressure drop ΔP_c^k of a Newtonian bubble employing $U_p^k = U_p(t = t_k)$ and $L_p^k = L_p(t = t_k)$ resulting from the previous time step;

(viii.b) Assuming that the plug moves at the average velocity between the two bubble tip velocities, i.e. $U_p = (U_r + U_f)/2$, the rear-bubble tip velocity at $t = t_k$ is computed as $U_r^k = 2U_p^k - U_f$, that leads to the rear-bubble capillary number;

(viii.c) Compute the capillary number for the bubble;

(viii.d) Compute the non-dimensional film thickness for a bubble advancing in a Newtonian fluid;

(viii.e) Compute the pressure drop at the rear-bubble tip ΔP_r^k for a Newtonian fluid;

(viii.f) Compute the Bingham and Deborah number of the rear bubble and use them to calculate the elastoviscoplastic correction $\varepsilon_r^k = \varepsilon_r^{EVP}$;

(viii.g) Compute the viscoplastic correction of ΔP_p^k by summing up all the Newtonian resistances (selecting either M1 or M2) and applying (9)(left);

(viii.h) Enforce a driving pressure difference across the plug, ΔP; combining the momentum and continuity equations, the time derivative of the plug velocity is expressed as

$$\frac{dU_p}{dt} = \frac{\Delta P - \Delta P_p^k}{\rho L_p^k} - \frac{U_p^k\left[\varepsilon_f(2-\varepsilon_f)U_f - \varepsilon_r^k(2-\varepsilon_r^k)U_r^k\right]}{L_p^k}; \tag{10}$$

9. Compute the variation in time of the liquid plug length by using the continuity equation:

$$\frac{dL_p}{dt} = \varepsilon_f(2-\varepsilon_f)U_f - \varepsilon_r^k(2-\varepsilon_r^k)U_r^k \tag{11}$$

10. Compute the time variation of the axial displacement by integrating the liquid plug velocity:

$$\frac{dZ_p}{dt} = U_p^k \tag{12}$$

11. Integrate the three ODEs and re-initialize U_p, L_p and Z_p before iterating from (viii.a) on.

The algorithm is initialized by setting $U_p(t = t_0)$, $L_p(t = t_0)$ and assuming $Z_p(t = t_0) = 0$.

3.4. Validation against experimental measurements and numerical simulations

The experimental validation of our reduced-order model is presented for two test fluids (0.25% and 1% of Actigum concentration) and three plug driving conditions per each test fluid. Owing to the limitations of the experimental apparatus in use, our equipment does not allow for an accurate control of the driving pressure ΔP and for a precise measurement of the front film thickness ε_f. These are three of the ten parameters of our reduced-order model, namely De, Bi, Ca, μ, ρ, L_0, $U_p(t = 0)$, a, ΔP, and ε_f.

All the parameters measured experimentally, i.e. De, Bi, Ca, μ, ρ, L_0, $U_p(t = 0)$, and a, are used in the model in order to compare the modeled and the experimental centerline plug dynamics. In our experiments, ΔP and ε_f are not measured, and they are therefore assumed as fitting parameters of our reduced-order model to match the experimental average plug speed $\overline{U}_p$.

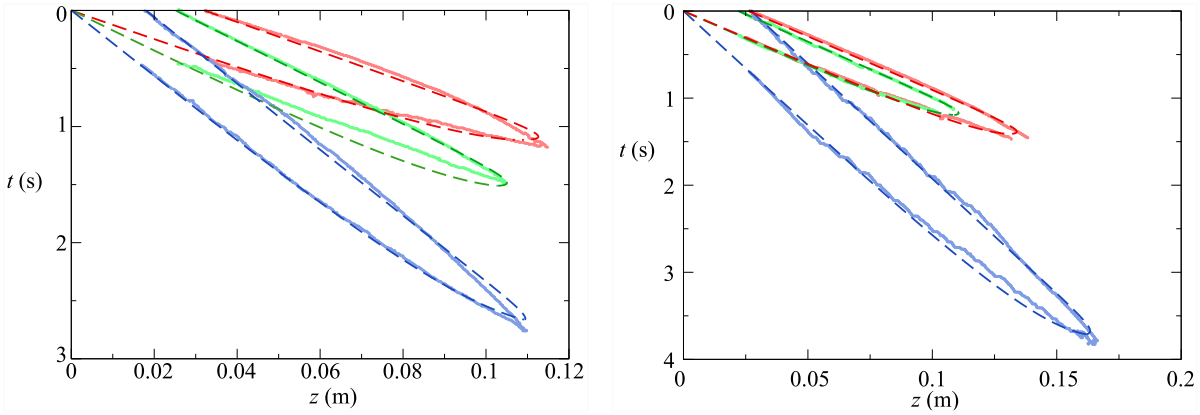

Fig. 10. Comparison between the space–time diagrams resulting from the reduced-order model (dashed line) and the experimental measurements (light-color markers) for Act. 0.25% (left) and Act. 1% (right). Three cases are compared for each concentration: blue (Case 1), green (Case 2), and red (Case 3).

Table 2
Parameters of the comparison between the experiments and the reduced-order model. Two concentrations are considered, i.e. Act. 0.25% and Act. 1%, for three driving conditions per test liquid (Cases 1 to 3).

Test Liquid	Parameter	Case 1	Case 2	Case 3
Act 0.25%	De_f	11.540	26.185	31.478
	Bi_f/Ca_f	5.981	3.004	2.570
	μ (Pa s)	0.0835	0.0670	0.0638
	ρ (kg/m^3)	990	990	990
	L_0 (m)	0.0180	0.0252	0.0322
	$U_p(t=0)$ (m/s)	0.0445	0.0783	0.0889
	a (m)	0.002	0.002	0.002
	ΔP (Pa)	216.0	287.0	437.0
	ϵ_f	0.145	0.165	0.195
Act 1.0%	De_f	63.667	141.394	196.953
	Bi_f/Ca_f	12.148	7.793	6.479
	μ (Pa s)	0.3168	0.2387	0.2123
	ρ (kg/m^3)	990	990	990
	L_0 (m)	0.0272	0.0222	0.0262
	$U_p(t=0)$ (m/s)	0.0481	0.0797	0.0983
	a (m)	0.002	0.002	0.002
	ΔP (Pa)	815.7	1029.5	1189.3
	ϵ_f	0.32	0.38	0.39

The parameters of our comparison are summarized in Table 2 for the six experiments considered. As shown in Fig. 10, the comparison between the dynamics predicted by the model and the experimental space–time diagram is satisfactory. We stress that only a narrow neighborhood of the selected parameter tuple (ΔP, ϵ_f) allows to reproduce the average plug speed of the experiments. Hence the degree of freedom of our parameter matching is very narrow, which shows that our quantitative matching is not made arbitrarily. Still, the model results are robust to small parameters variations. We further stress that, based on the results of Fig. 10 the non-linear interplay between viscoelasticity and viscoplasticity seems to play a significant role only in the final phase of the rupture, when the interface curvature (partially neglected in our model) must also play a significant role. We also expect that local interesting features are determined by the complex rheology of the fluid, but their investigation would require detailed simulations and experimental techniques which are out of the scope of our study.

A second validation of our reduced-order model is carried out by comparing the conditions of steady propagation for a viscoplastic liquid plug. The results of Zamankhan et al. [47] are assumed as reference, as they result form the numerical simulation of a two-dimensional Stokes flow for a viscoplastic liquid plug. Fig. 11 depicts the comparison

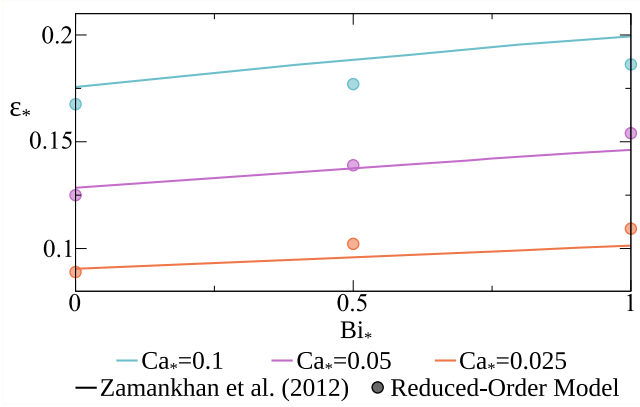

Fig. 11. Comparison between the equilibrium non-dimensional film thickness from the reduced-order model (markers) and the numerical simulations (lines) for $Ca_* = 0.1$ (light-blue), 0.05 (violet), and 0.025 (orange). The Bingham number is varied to determine the equilibrium conditions for the propagation of a viscoplastic liquid plug.

between our reduced order model (markers), and the full numerical simulations of Zamankhan et al. [47] (lines) for $Ca_* = 0.1$, 0.05, and 0.025. The equilibrium film thickness to achieve a steady plug propagation is well predicted by our reduced-order model for the whole interval of Bingham numbers considered $Bi_* \in [0,\ 1]$. The differences between the model results and the numerical simulations are partially due to the difference in the geometrical set-up, as our reduced-order model assumes an axisymmetric flow, while Zamankhan et al. solve the steady liquid plug flow in a plane channel.

3.5. Parametric study on the standalone non-Newtonian non-dimensional groups

The reduced-order model formulated in Section 3 is here employed to investigate the effect of viscoelasticity and viscoplasticity. Since these two effects have been superposed in the model equations proposed in Section 3.3, we will consider them separately in the following subsections. In this parametric study, we will employ our reduced-order model to characterize the trends of L_r and t_r upon a change of Ca/Bi, and De for physiologically-relevant regimes that exceed the parameters range investigated experimentally.

All the following results presented in Section 3.5.1 and 3.5.2 are obtained for the same baseline clean Newtonian set-up, indicated as the solid black line in Figs. 12 and 13. The baseline parameters are: $\epsilon_f = 0.05$, $\mu = 0.005$ Pa s, $\rho = 1000$ kg/m^3, $\sigma = 0.070$ N/m, $a = 0.005$ m, $L_p(t = 0) = 0.1$ m, $U_p(t = 0) = 0.01$ m/s and $\Delta P = 150$ Pa. All

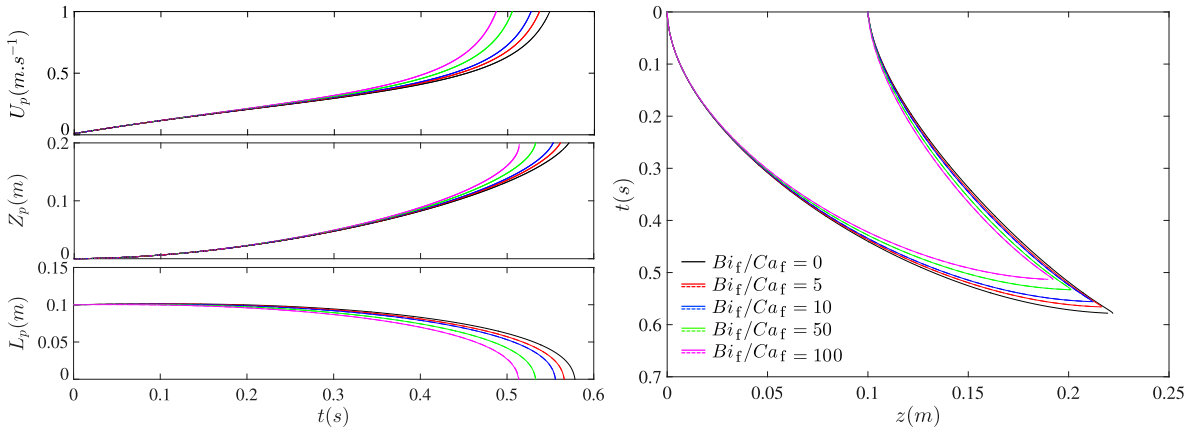

Fig. 12. Effect of the viscoplastic rheological properties on the liquid plug rupture. The Newtonian case ($Bi_f/Ca_f = 0$) is depicted in black solid line, while the viscoplastic cases are shown in red ($Bi_f/Ca_f = 5$), blue ($Bi_f/Ca_f = 10$), green ($Bi_f/Ca_f = 50$) and magenta ($Bi_f/Ca_f = 100$). In all simulations, we set $\epsilon_f = 0.05$, $\mu = 0.005$ Pa s, $\rho = 1000$ kg/m^3, $\sigma = 0.070$ N/m, $a = 0.005$ m, $L_p(t = 0) = 0.1$ m, $U_p(t = 0) = 0.01$ m/s, $\Delta P = 150$ Pa, $De_f = 0$ and $\beta = 0$. The two versions of the reduced-order model for clean plugs are tested: M1 (dashed lines), M2 (solid lines). Left panels: Liquid plug dynamics in terms of plug velocity U_p, traveling distance Z_p, and length L_p. Right panel: spatio-temporal diagram of the plug rear and front meniscus tips.

simulations are carried out until plug rupture by integrating the ODEs of Section 3 by an explicit Euler method and employing $\Delta t = 0.001$ s as time step.

3.5.1. Effect of viscoplasticity

The effect of viscoplasticity is taken into account by increasing the leading plug resistance and the film thickness as shown in Fig. 12. The increase of liquid plug resistance has a direct effect on the liquid plug by decelerating it. On the other hand, the increase of film thickness reduces the menisci curvatures, reducing the capillary resistance of the plug and inducing an acceleration of the plug. We stress that in this and in the following subsections we use our reduced-order model to isolate the effect of Bi_f/Ca_f on the pressure drop and the film thickness, and we compare with Newtonian plugs keeping the dynamic viscosity constant. The goal of such an analysis is to better understand the net deceleration of the liquid plug observed for higher yield stresses (see Fig. 10). For $Bi_f/Ca_f \in [0, 100]$, the latter effect prevails and the liquid plug experiences a net acceleration. Keeping the leading film thickness constant, for a given Bi_f/Ca_f the velocity of the leading meniscus tip is fixed and an increase of the plug velocity increases the rear capillary number. This implies that the rear film thickness increases because of both, the Newtonian (4) and the viscoplastic effects (9). For $Bi_f/Ca_f \in [0, 100]$, therefore, the viscoplastic liquid plug deposits more liquid than a Newtonian one (of same effective dynamic viscosity) due to the increased trailing film thickness and, as a consequence, the rupture occurs at a shorter rupture time t_r. Despite the fact that U_p for a viscoplastic liquid plug is higher than that for a Newtonian plug, both, the rupture time t_r and the traveled distance Z_p decrease upon an increase of Bi_f/Ca_f keeping the effective dynamic viscosity constant. This is demonstrated in Fig. 12, where the results obtained for several Bingham-to-capillary-number ratios are shown, i.e. $Bi_f/Ca_f = 0$ (black, Newtonian), $Bi_f/Ca_f = 5$ (red), $Bi_f/Ca_f = 10$ (blue), $Bi_f/Ca_f = 50$ (green), and $Bi_f/Ca_f = 100$ (magenta). The two variants M1 (dashed lines) and M2 (solid lines) are also compared in Fig. 12 showing that our reduced-order model is insensitive to the two matching corrections tested.

3.5.2. Effect of viscoelasticity

The effect of viscoelasticity on the liquid plug rupture is taken into account by an increase of leading and trailing film thickness defined by (8). Keeping the leading film thickness constant, for a given De_f, the tip velocity of the retracting air bubble is fixed and the viscoplastic liquid plug deposits more liquid than the Newtonian one because of the increased trailing film thickness. Hence, the plug rupture occurs at shorter rupture times t_r, keeping constant the effective dynamic viscosity. Depositing more liquid on the wall, the plug reduces the curvature and, consequently, the capillary pressure resistance. This leads to increase the velocity of the plug upon an increase of De_f. Despite such an increase, the shortening of the rupture time plays a dominant role in the plug dynamics and leads to a reduction of the distance traveled by the liquid plug before rupture, Z_p. This liquid plug dynamics is demonstrated in Fig. 13 for $De_f \in [0, 100]$. The results are obtained for several Deborah numbers including $De_f = 0$ (black, Newtonian), $De_f = 5$ (red), $De_f = 10$ (blue), $De_f = 50$ (green), and $De_f = 100$ (magenta). The liquid–gas interface is assumed to be clean, and the models M1 (dashed lines) and M2 (solid lines) are compared. The quantitative differences between the corresponding results are less than 20% and the qualitative trends of the two variants of our reduced-order model provide a consistent prediction. We stress that these results are not intended for a direct comparison with the experimental measurements since the experiments are not carried out at constant ΔP, μ, ϵ_f, $L_p(t = 0)$, as we do for producing the model results in Section 3.5.

4. Summary and conclusions

The rupture of a non-Newtonian liquid plug in a capillary tube has been investigated for reproducing the airway reopening in the 6th-to −7th generation of adult human lungs. Four synthetic mucus samples are used to study the elastoviscoplastic effect of the liquid on the plug rupture ranging over several orders of magnitude for the Deborah, Bingham and capillary numbers. A detailed rheological characterization of our liquid samples have been provided, including the determination of the model parameters for the Herschel–Bulkley model (viscoplasticity) and the White–Metzner model (viscoelasticity). Shear relaxation time measurements were carried out, as they are commonly employed in the literature for characterizing the relaxation time of biological and synthetic mucus [70,71]. However, considering the extensional rheology would be also of interest as the polymeric stretching plays a significant role during the liquid plug rupture. Future studies will therefore focus on measuring the extensional viscosity and relaxation time of mucus in order to better relate the plug dynamics to the fluid rheology.

In support to our experiments, we derived an original reduced-order model built on the existing literature. Our model takes into account the effect of viscoplasticity and viscoelasticity, assuming they can be linearly superposed.

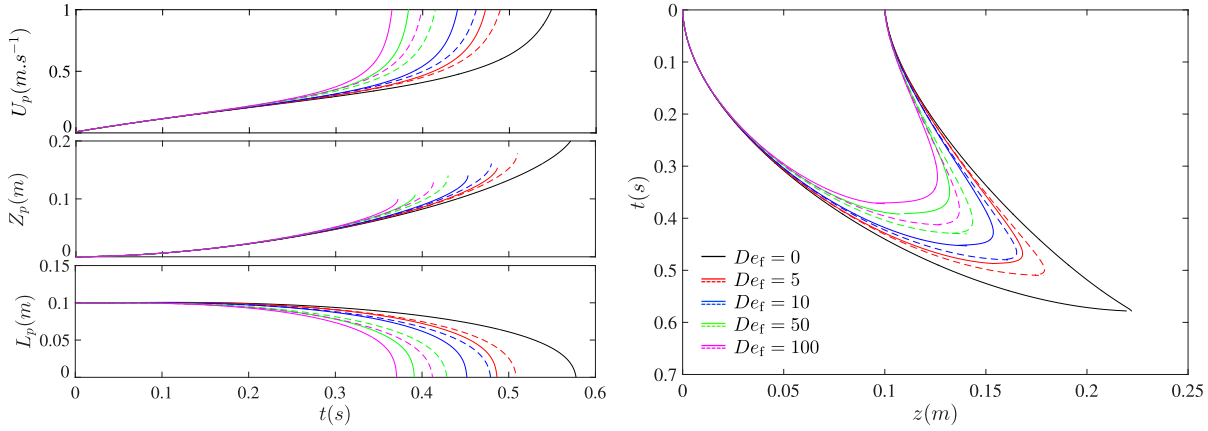

Fig. 13. Effect of the viscoelastic rheological properties on the liquid plug rupture. The Newtonian case ($De_f = 0$) is depicted in black solid line, while the viscoelastic cases are shown in red ($De_f = 5$), blue ($De_f = 10$), green ($De_f = 50$) and magenta ($De_f = 100$). In all simulations, we set $\epsilon_f = 0.05$, $\mu = 0.005$ Pa s, $\rho = 1000$ kg/m^3, $\sigma = 0.070$ N/m, $a = 0.005$ m, $L_p(t = 0) = 0.1$ m, $U_p(t = 0) = 0.01$ m/s, $\Delta P = 150$ Pa, $Bi_f/Ca_f = 0$ and $\beta = 0$. The two versions of the reduced-order model for clean plugs are tested: M1 (dashed lines), M2 (solid lines). Left panels: Liquid plug dynamics in terms of plug velocity U_p, traveling distance Z_p, and length L_p. Right panel: spatio-temporal diagram of the plug rear and front meniscus tips.

By means of space–time diagrams, we quantitatively characterize the dynamics of the liquid plug along the centerline of the pipe. Upon a decrease of $\overline{U}_p$ we observe a correlated increase of the rupture time, while μ, λ, and τ_0 are rather impactful on the dimensionless traveling length $L_r/(L_i - L_f)$, that increases as $\mu \uparrow$, $\lambda \uparrow$, and $\tau_0 \uparrow$. These same trends are predicted by our reduced-order model, when validating against the experiments. Our reduced-order model has also been used to isolate the viscoplastic effect from the viscoelasticity of mucus, taking into account the increase of the film thickness and of the pressure drop due to viscoplasticity (9).

Comparing the synthetic mucus samples at different Actigum concentrations, our experiments uncovered a remarkable axi-symmetry breaking for the liquid plugs at high Bi and De. As a result, the liquid plug does not rupture along the centerline, on the contrary of what has always been observed for almost-Newtonian liquids (MUC-0.25% and MUC-0.5%) in our experiment. This non-Newtonian effect is in agreement with the experimental results of Caliman et al. [60], who unravel the various regimes of symmetry breaking for viscoplastic fluids in capillary pipes.

Our model prediction, corroborated by the experimental evidence, shows that a standalone increase of Bi/Ca and of De on the liquid film thickness and plug resistance can facilitate liquid plug rupture, compared to Newtonian plugs of equal effective viscosity. This conclusions help interpreting the experimental findings by identifying the contribution of single non-dimensional groups. Upon an increase of Actigum concentration, for a given $\overline{U}_p$, $\overline{Ca} \uparrow$, $\overline{Bi} \uparrow$, and $\overline{De} \downarrow$ (where the overline denotes the non-dimensional groups computed using $\overline{U}_p$, see Table 2). For comparable $\overline{U}_p$, (the same case labeling in Table 2), the dimensional rupture time is not significantly affected (the same colors in Fig. 10). This, in combination with the one-order-of-magnitude increase of μ upon an increase of concentration from MUC-0.5% and MUC-1.5% (see Table 2), explains why the non-dimensional rupture time in capillary time units ($t\sigma/\mu a$) decreases upon an increase of $\overline{De}$ and a decrease of $\overline{Ca}$ and $\overline{Bi}$, as observed experimentally. On the other hand, the dimensional rupture time increases upon an increase of non-Newtonian effects due to a higher effective viscosity. This same trend has been reproduced by our reduced-order model (see Table 2) and is consistent with the medical literature, that reports a significant enhancement of the dimensional rupture time and plug resistance in patients affected by asthma [72]. In fact, increasing the polymeric concentration leads to a net increased difficulty of reopening the airways and a higher pressure driving must be applied to rupture the mucus liquid plugs in patients affected by asthma in order to allow air exchange at distal airways.

These conclusive considerations suggest the future studies should focus on including the non-linear interaction between complex rheological effects, as well as on validating the predictions of our reduced-order model, either by numerical simulations or by experiments.

Declaration of competing interest

The authors declare that they have no known competing financial interests or personal relationships that could have appeared to influence the work reported in this paper.

Data availability statement

The data that support the findings of this study are available from the corresponding author upon reasonable request.

Acknowledgments

Support from National Institutes of Health (NIH), USA, grant number R01-HL136141, and the Scientific and Technical Research Council of Turkey, (TUBITAK), grant number 119M513, is kindly acknowledged.

Appendix. Conservation laws

The second and third equations of (3) are here derived starting from first principles. The cross-section-averaged conservation of momentum in the liquid plug reads

$$\rho \frac{d(V_p U_p)}{dt} = \pi a^2 \left(\Delta P - \Delta P_p\right), \tag{A.1}$$

where V_p is the plug volume approximated as $V_p = \pi a^2 L_p$. Simplifying the constant factor common to all terms of the equation, i.e. πa^2, and dividing by the liquid density, it yields

$$\frac{d(L_p U_p)}{dt} = \frac{\Delta P - \Delta P_p}{\rho}. \tag{A.2}$$

Finally, re-arranging the l.h.s. and substituting the liquid plug pressure drop with the corresponding plug resistance times the flow rate ($\Delta P_p = \pi a^2 R_p U_p$), the one-dimensional Navier–Stokes equation reads

$$U_p \frac{dL_p}{dt} + L_p \frac{dU_p}{dt} = \frac{\Delta P - \pi a^2 R_p U_p}{\rho}, \tag{A.3}$$

which is equivalent to the second equation of (3), where the first term of the l.h.s. has been moved to the r.h.s. and we divided all the term of the equation by L_p.

The last equation of (3) is derived by the cross-section-averaged conservation of mass for the liquid phase. Considering a control volume between the trailing and the leading film, the one-dimensional conservation of mass reads

$$\rho \frac{dV_p}{dt} = \rho\pi \left[a^2 - \left(a - h_f\right)^2\right] U_f - \rho\pi \left[a^2 - \left(a - h_r\right)^2\right] U_r. \tag{A.4}$$

Substituting the plug volume with $V_p = \pi a^2 L_p$ and dividing by $\rho\pi a^2$, the conservation of mass reads

$$\frac{dL_p}{dt} = \left[1 - \left(1 - \varepsilon_f\right)^2\right] U_f - \left[1 - \left(1 - \varepsilon_r\right)^2\right] U_r, \tag{A.5}$$

which is equivalent to the last equation of (3).

References

[1] D. Tsaoulidis, V. Dore, P. Angeli, N.V. Plechkova, K.R. Seddon, Flow patterns and pressure drop of ionic liquid–water two-phase flows in microchannels, Int. J. Multiph. Flow 54 (2013) 1–10.

[2] A. Kazemi, B. Louis, D. Isabey, G.F. Nieman, L.A. Gatto, J. Satalin, S. Baker, J.B. Grotberg, M. Filoche, Surfactant delivery in rat lungs: Comparing 3D geometrical simulation model with experimental instillation, PLoS Comput. Biol. 15 (10) (2019) e1007408.

[3] J. Widdicombe, S. Bastacky, D. Wu, C. Lee, Regulation of depth and composition of airway surface liquid, Eur. Respir. J. 10 (12) (1997) 2892–2897.

[4] J. Plateau, Statique expérimentale et théorique des liquides soumis aux seules forces moléculaires (Vol. 2), Gauthier-Villars, 1873.

[5] L. Rayleigh, On the capillary phenomena of jets, Proc. R. Soc. Lond. 29 (1879) 71–97.

[6] R.D. Kamm, R.C. Schroter, Is airway closure caused by a liquid film instability? Respir. Physiol. 75 (1989) 141–156.

[7] P.T. Macklem, Airway obstruction and collateral ventilation, Physiol. Rev. 51 (1971) 368–436.

[8] A. Gunther, C. Siebert, R. Schmidt, S. Ziegler, F. Grimminger, M. Yabut, B. Temmesfeld, D. Walmrath, H. Morr, W. Seeger, Surfactant alterations in severe pneumonia, acute respiratory distress syndrome, and cardiogenic lung edema, Am. J. Resp. Crit. Care 153 (1996) 176–184.

[9] J. Veen, A.J. Beekman, E.H. Bel, P.J. Sterk, Recurrent exacerbations in severe asthma are associated with enhanced airway closure during stable episodes, Am. J. Respir. Crit. Care Med. 161 (6) (2000) 1902–1906.

[10] P.A. Dargaville, M. South, P.N. Mcdougall, Surfactant abnormalities in infants with severe viral bronchiolitis, Arch. Dis. Child. 75 (1996) 133–136.

[11] C. Guerin, S. Lemasson, R. de Varax, J. Milic-Emili, G. Fournier, Small airway closure and positive end-expiratory pressure in mechanically ventilated patients with chronic obstructive pulmonary disease, Am. J. Resp. Crit. Care 155 (1997) 1949–1956.

[12] M. Griese, R. Essl, R. Schmidt, E. Rietschel, F. Ratjen, M. Ballmann, K. Paul, Pulmonary surfactant, lung function, and endobronchial inflammation in cystic fibrosis, Am. J. Respir. Crit. Care Med. 170 (9) (2004) 1000–1005.

[13] C.S. Baker, T.W. Evans, B.J. Randle, P.L. Haslam, Damage to surfactant-specific protein in acute respiratory distress syndrome, Lancet 353 (1999) 1232–1237.

[14] S. Bian, C.F. Tai, D. Halpern, Y. Zheng, J.B. Grotberg, Experimental study of flow fields in an airway closure model, J. Fluid Mech. 647 (2010) 391–402.

[15] C.F. Tai, S. Bian, D. Halpern, Y. Zheng, M. Filoche, J.B. Grotberg, Numerical study of flow fields in an airway closure model, J. Fluid Mech. 677 (2011) 483–502.

[16] F. Romanò, H. Fujioka, M. Muradoglu, J.B. Grotberg, Liquid plug formation in an airway closure model, Phys. Rev. Fluids 4 (2019) 093103.

[17] J.B. Grotberg, Crackles and wheezes: agents of injury? Ann. Am. Thorac. Soc. 16 (8) (2019) 967–969.

[18] K.J. Cassidy, Liquid Film Dynamics in the Pulmonary Airways, (Ph.D. thesis), Northwestern University, 1999.

[19] D. Halpern, H. Fujioka, S. Takayama, J.B. Grotberg, Liquid and surfactant delivery into pulmonary airways, Respir Physiol. Neurobiol. 163 (2008) 222–231.

[20] D. Halpern, J.B. Grotberg, Fluid-elastic instabilities of liquid-lined flexible tubes, J. Fluids Mech. 244 (1992) 615–632.

[21] M. Heil, A.L. Hazel, J.A. Smith, The mechanics of airway closure, Respir Physiol. Neurobiol. 163 (2008) 214–221.

[22] D.B. Yeates, R.G. Crystal, J.B. West, The Lung: Scientific Fundations - Mucus Rheology, Raven Press, Ltd, 1990, pp. 197–203.

[23] F. Romanò, M. Muradoglu, H. Fujioka, J.B. Grotberg, The effect of viscoelasticity in an airway closure model, J. Fluid Mech. 913 (2021) A31.

[24] M.S. Quraishi, N.S. Jones, J. Mason, The rheology of nasal mucus: A review, Clin. Otolaryngol. 23 (5) (1998) 403–413.

[25] D. Halpern, H. Fujioka, J.B. Grotberg, The effect of viscoelasticity on the stability of a pulmonary airway liquid layer, Phys. Fluids 22 (2010) 011901.

[26] D. Halpern, J.B. Grotberg, Nonlinear saturation of the Rayleigh instabilitydue to oscillatory flow in a liquid-lined tube, J. Fluids Mech. 492 (2003) 251–270.

[27] H. Fujioka, J.B. Grotberg, Steady propagation of a liquid plug in a two-dimensional channel, J. Biomech. Eng. 126 (2004) 567–577.

[28] J. Grotberg, Respiratory fluid mechanics, Phys. Fluids (2011) 021301.

[29] P. Piirila, A.R.A. Sovijarvi, Crackles: Recording, analysis and clinical significance, Eur. Respir. J. 8 (1995) 2139–2148.

[30] F.P. Bretherton, The motion of long bubbles in tubes, J. Fluid Mech. 10 (1961) 166–188.

[31] G.I. Taylor, Deposition of a viscous fluid on the wall of a tube, J. Fluid Mech. 10 (1961) 161–165.

[32] D. Huh, H. Fujioka, Y.C. Tung, N. Futai, R.P. III, J.B. Grotberg, Acoustically detectable cellular-level lung injury induced by fluid mechanical stresses in microfluidic airway systems, Proc. Natl. Acad. Sci. USA 104 (2007) 18886–18891.

[33] A.M. Bilek, K.C. Dee, D.P. Gaver, Mechanisms of surface-tension-induced epithelial cell damage in a model of pulmonary airway reopening, J. Appl. Physiol. 94 (2003) 770–783.

[34] S.S. Kay, A.M. Bilek, K.C. Dee, D.P. Gaver, Pressure gradient, not exposure duration, determines the extent of epithelial cell damage in a model of pulmonary airway reopening, J. Appl. Physiol. 97 (2004) 269–276.

[35] H. Fujioka, J.B. Grotberg, The steady propagation of a surfactant-laden liquid plug in a two-dimensional channel, Phys. Fluids 17 (2005) 082102.

[36] H. Fujioka, S. Takayama, J.B. Grotberg, Unsteady propagation of a liquid plug in a liquid-lined straight tube, Phys. Fluids 20 (2008) 062104.

[37] E.A. Hassan, E. Uzgoren, H. Fujioka, J.B. Grotberg, W. Shyy, Adaptive Lagrangian-Eulerian computation of propagation and rupture of a liquid plug in a tube, Internat. J. Numer. Methods Fluids 67 (2011) 1373–1392.

[38] M. Muradoglu, F. Romanò, H. Fujioka, J.B. Grotberg, Effects of surfactant on propagation and rupture of a liquid plug in a tube, J. Fluid Mech. 872 (2019) 407–437.

[39] J.G. Muscedere, J.B.M. Mullen, K. Gan, A.S. Slutsky, Tidal ventilation at low airway pressures can augment lung injury, Am. J. Resp. Crit. Care 149 (1994) 1327–1334.

[40] V. Taskar, J. John, E. Evander, B. Robertson, B. Jonson, Surfactant dysfunction makes lungs vulnerable to repetitive collapse and reexpansion, Am. J. Resp. Crit. Care 155 (1997) 313–320.

[41] D. Halpern, J.B. Grotberg, Surfactant effects on fluid-elastic instabilities of liquid-lined flexible tubes: A model of airway closure, J. Biomech. Eng. 115 (1993) 271–277.

[42] H. Tavana, P. Zamankhan, P.J. Christensen, J.B. Grotberg, S. Takayama, Epithelium damage and protection during reopening of occluded airways in a physiologic microfluidic pulmonary airway model, Biomed. Microdevices 13 (2011) 731–742.

[43] Y. Zheng, H. Fujioka, S. Bian, Y. Torisawa, D. Huh, S. Takayama, J.B. Grotberg, Liquid plug propagation in flexible microchannels: A small airway model, Phys. Fluids 21 (2009) 071903.

[44] Y. Hu, S. Bian, J. Grotberg, M. Filoche, J. White, S. Takayama, J.B. Grotberg, A microfluidic model to study fluid dynamics of mucus plug rupture in small lung airways, Biomicrofluidics 9 (2015) 044119.

[45] Y. Hu, F. Romanò, J.B. Grotberg, Effects of surface tension and yield stress on mucus plug rupture: A numerical study, J. Biomech. Eng. 142 (6) (2020).

[46] H.T. Low, Y.T. Chew, C.W. Zhou, Pulmonary airway reopening: Effects of non-Newtonian fluid viscosity, J. Biomech. Eng. 119 (1997) 298–308.

[47] P. Zamankhan, B.T. Helenbrook, S. Takayama, J.B. Grotberg, Steady motion of bingham liquid plugs in two-dimensional channels, J. Fluid Mech. 705 (2012) 258–279.

[48] M. Baudoin, Y. Song, P. Manneville, C.N. Baroud, Airway reopening through catastrophic events in a hierarchical network, Proc. Natl. Acad. Sci. USA 110 (2013) 859–864.

[49] M. Filoche, C.F. Tai, J.B. Grotberg, Three-dimensional model of surfactantreplacement therapy, Proc. Natl. Acad. Sci. USA 112 (2015) 9287–9292.

[50] J.B. Grotberg, Pulmonary flow and transport phenomena, J. Fluids Mech. 26 (1994) 529–571.

[51] J.B. Grotberg, Respiratory fluid mechanics and transport processes, Annu. Rev. Biomed. Eng 3 (2001) 421–457.

[52] O. Lafforgue, I. Seyssiecq, S. Poncet, J. Favier, Rheological properties of synthetic mucus for airway clearance, J. Biomed. Mat. Res. Part A 106 (2) (2018) 386–396.

[53] S. Ahmadikhamsi, F. Golfier, C. Oltean, E. Lefevre, S.A. Bahrani, Impact of surfactant addition on non-Newtonian fluid behavior during viscous fingering in Hele-Shaw cell, Phys. Fluids 32 (2020) 012103.

[54] S.A. Bahrani, C. Nouar, Intermittency in the transition to turbulence for a shear-thinning fluid in hagen-poiseuille flow, J. Appl. Fluid Mech. 7 (2014) 1–6.

[55] L. Casanellas, M.A. Alves, R.J. Poole, S. Lerouge, A. Lindner, The stabilizing effect of shear thinning on the onset of purely elastic instabilities in serpentine microflows, Soft Matter 12 (2016) 6167–6175.

[56] J.L. White, A.B. Metzner, Development of constitutive equations for polymeric melts and solutions, J. Appl. Polym. Sci. 7 (5) (1963) 1867–1889.

[57] R.H. Ewoldt, M.T. Johnston, L.M. Caretta, Experimental challenges of shear rheology: How to avoid bad data, in: Complex Fluids in Biological Systems: Experiment, Theory, and Computation, Springer, New York, 2015, pp. 207–241.
[58] C.W. Macosko, Rheology: Principles, Measurements, and Applications, VCH Publishers, Macosko1994, 1994, p. 568.
[59] W.T. Vetterling, S.A. Teukolsky, W.H. Press, B.P. Flannery, Numerical Recipes in Fortran, Cambridge University Press, 1992.
[60] H.M. Caliman, E.J. Soares, R.L. Thompson, An experimental investigation on the Newtonian–Newtonian and viscoplastic–Newtonian displacement in a capillary tube, J. Non-Newton. Fluid Mech. 247 (2017) 207–220.
[61] P.D. Howell, S.L. Waters, J.B. Grotberg, The propagation of a liquid bolus along a liquid-lined flexible tube, J. Fluids Mech. 406 (2000) 309–335.
[62] S.L. Waters, J.B. Grotberg, The propagation of a surfactant laden liquid plug in a capillary tube, Phys. Fluids 14 (2002).
[63] H. Fujioka, D. Halpern, J. Ryans, D.P. Gaver III, Reduced-dimension model of liquid plug propagation in tubes, Phys. Rev. Fluids 1 (5) (2016) 053201.
[64] P. Aussillous, D. Quéré, Quick deposition of a fluid on the wall of a tube, Phys. Fluids 12 (10) (2000) 2367–2371.
[65] Z. Che, T.N. Wong, N.T. Nguyen, An analytical model for plug flow in micro-capillaries with circular cross section, Int. J. Heat Fluid Flow 32 (5) (2011) 1005–1013.
[66] V. Gauri, K.W. Koelling, The motion of long bubbles through viscoelastic fluids in capillary tubes, Rheol. Acta 38 (5) (1999) 458–470.
[67] P. Zamankhan, S. Takayama, J.B. Grotberg, Steady displacement of long gas bubbles in channels and tubes filled by a bingham fluid, Phys. Rev. Fluids 3 (1) (2018) 013302.
[68] B. Laborie, F. Rouyer, D.E. Angelescu, E. Lorenceau, Yield-stress fluid deposition in circular channels, J. Fluid Mech. 818 (2017) 838–851.
[69] M. Jalaal, N.J. Balmforth, Long bubbles in tubes filled with viscoplastic fluid, J. Non-Newton. Fluid Mech. 238 (2016) 100–106.
[70] S.K. Lai, Y.Y. Wang, D. Wirtz, J. Hanes, Micro- and macrorheology of mucus, Adv. Drug Deliv. Rev. 61 (2009) 86–100.
[71] J. Patarin, E. Ghiringhelli, G. Darsy, M. Obamba, P. Bochu, B. Camara, S. Quétant, J.-L. Cracowski, C. Cracowski, M. Robert de Saint Vincent, Rheological analysis of sputum from patients with chronic bronchial diseases, Sci. Rep. 10 (2020) 15685.
[72] E.M. Dunican, B.M. Elicker, D.S. Gierada, S.K. Nagle, M.L. Schiebler, J.D. Newell, W.W. Raymond, M.E. Lachowicz-Scroggins, S. Di Maio, E.A. Hoffman, et al., Mucus plugs in patients with asthma linked to eosinophilia and airflow obstruction, The Journal of Clinical Investigation 128 (3) (2018) 997–1009.